OPEN ACCESS
IOP PUBLISHING
SCIENCE AND TECHNOLOGY OF ADVANCED MATERIALS
Sci. Technol. Adv. Mater. **14** (2013) 035006 (12pp)
doi:10.1088/1468-6996/14/3/035006

Extruded blend films of poly(vinyl alcohol) and polyolefins: common and hard-elastic nanostructure evolution in the polyolefin during straining as monitored by SAXS

Norbert Stribeck[1], Ahmad Zeinolebadi[1,4], Stoyko Fakirov[2], Debes Bhattacharyya[2] and Stephan Botta[3]

[1] Department of Chemistry, University of Hamburg, Bundesstrasse. 45, D-20146 Hamburg, Germany
[2] Mechanical Engineering Department, University of Auckland, Private Bag 92019, Auckland, New Zealand
[3] HASYLAB at DESY, Notkestrasse. 85, D-22603 Hamburg, Germany

E-mail: norbert@stribeck.de

Received 15 March 2013
Accepted for publication 29 April 2013
Published 5 June 2013
Online at stacks.iop.org/STAM/14/035006

Abstract
Straining of PVA/PE and PVA/PP blends (70 : 30) is monitored by small-angle x-ray scattering (SAXS). Sheet-extruded films with different predraw ratio are investigated. The discrete SAXS of predrawn samples originates from polyolefin nanofibrils inside of polyolefin microfibrils immersed in a PVA matrix. PE nanofibrils deform less than the macroscopic strain without volume change. PP nanofibrils experience macroscopic strain. They lengthen but their diameter does not decrease. This is explained by strain-induced crystallization of PP from an amorphous depletion shell around the core of the nanofibril. The undrawn PVA/PE film exhibits isotropic semicrystalline nanostructure. Undrawn PVA/PP holds PP droplets containing oriented stacks of semicrystalline PP like neat precursors of hard-elastic thermoplasts. Respective predrawn films are softer than the undrawn material, indicating conversion into the hard-elastic state. Embedding of the polyolefin significantly retards neck formation. The polyolefin microfibrils can easily be extracted from the water-soluble matrix.

Keywords: blend polymer film, straining, small-angle x-ray scattering, microstructure, mechanical properties, hard-elastic

1. Introduction

Drawing an extruded blend of two polymers causes the droplets of the embedded polymer to be reshaped into elongated entities. In this way highly extended microfibrils [1] of the embedded polymer can be generated inside the matrix polymer. The aim of this work has been to study the nanostructure that is generated by this conversion process. In many cases it is possible to wash out the matrix polymer using an organic solvent and thus to gain microfibrils for special applications. Particularly interesting is the use of microfibrils as scaffold for tissue engineering. In this field, even traces of organic solvents in the scaffolds have a negative effect on the cell growth. If the matrix polymer is water-soluble,

[4] Present address: Polymer Consult GmbH, Dorfgrund 6, D-22397 Hamburg, Germany.

it is easily extracted. No organic solvent is required. Such a matrix polymer is poly(vinyl alcohol) (PVA or PVOH). Polypropylene (PP) microfibrils resulting from such a process have been presented by Ku and Lin [2]. Their typical diameter ranges between 1 and 10 μm. Replacing organic solvents with water makes the extraction method environmentally friendly and cost effective, because the water-soluble polymer can be regenerated and reused. Moreover, materials made in a water-based process are particularly attractive for biomedical applications.

As a matrix, we use commercial thermoplastic poly(vinyl alcohol) (PVA or PVOH). Encapsulated into it is either polyethylene (PE) or PP. PVA is peculiar both in processing and morphology concerns. As a consequence, neat and dry PVA cannot be extruded, because hydrogen bonds are formed inside its crystals. So-called thermoplastic grades of PVA contain a plasticizer [2, 3]. In general, this is a polyhydric alcohol [4] which reduces the melting point and affects the crystallization behavior [5]. Although commercial PVA is atactic [6], it can crystallize because the hydroxyl group is small [7, 8]. Nevertheless, the packing of the atoms in the crystals is not much denser than in the amorphous state. Thus PVA is a weak scatterer of x-rays at small angles, because the contrast between the amorphous phase and the crystalline phase is very low. Consequently, there are few small-angle x-ray scattering (SAXS) studies on PVA. The poor contrast can be enhanced by swelling the films in water [9], or by switching from x-rays to neutrons [10, 11]. Remaining options for the study of dry PVA by SAXS are the investigation of microvoids [12] or an undisturbed monitoring of foreign embedded components with respect to their nanostructure.

In the present study we use the SAXS to monitor blends during homogeneous straining. The samples are dry films of PVA blended with polyolefins. Necking of the films limits the range in which a unique relation holds between macroscopic strain and the nanostructure data. Therefore films with different predraw ratio are prepared and studied. In this way we expect to cover a long interval of strains. Ultimately we aim at the identification and description of the mechanisms by which the semicrystalline structure of the polyolefin is responding to the strain. As has been done in a previous study [13] we discriminate between the microfibrils that are visible in the scanning electron microscope (SEM) and the fibrillar structure on the nanometer scale ('nanofibril') that is probed by the SAXS.

Commonly, extruded thermoplasts are macroscopically isotropic because they have undergone spherulitic crystallization. On the scale of nanometers the spherulite is made from stacks of semicrystalline layers. On the other hand, highly oriented semicrystalline nanofibrils of granular-shaped crystallites are generated, if the molecular mass of the polyolefin is very high and the processing is performed under extreme temperature and pressure gradients. In the intermediate [14] range a peculiar highly-oriented, layered semicrystalline nanostructure is found. It is commonly called 'precursor of a hard-elastic thermoplast' (PHET). Although well known with neat polymers, to our knowledge such a structure has never been observed in the minority fraction of a blend. Hard-elastic films from thermoplasts [14–18] are commercially produced and converted into microporous membranes that are, e.g., used as battery separators or ultrafiltration membranes.

2. Experimental details

2.1. Materials

The studied materials are blends from polyvinyl alcohol (PVA) and a reinforcing polyolefin. The composition of the samples is identical, 70 wt% PVA and 30 wt% of the polyolefin.

The thermoplastic PVA is the commercial extrusion grade ®Mowiflex TC 232 made by Kuraray Co, Ltd. It is plasticized [19]. Its melt-flow index (MFI) (190 °C, 21.6 kg) is 39 ± 8 g per 10 min, glass transition temperature $T_g = 34$ °C, melt temperature $T_m = 178$ °C [20]. Reported [21] mass density of Mowiflex TC 232: $\rho = 1.27$ g cm^{-3}. For neat PVA the reported [7] amorphous density $\rho_a = 1.268$ g cm^{-3} and crystalline density $\rho_c = 1.345$ g cm^{-3} are close to each other.

Two types of reinforcing polyolefins are used. The first grade is a polyethylene (PE), more specifically the linear low density polyethylene (LLDPE) QAMAR FC 21 HN® by Eastern Petrochemical Company SHARQ, Saudi Arabia, with a MFI = 1.0 g per 10 min and $T_m = 122$ °C. It was selected because of its excellent drawability. For simplicity we will address this polyolefin by the abbreviation PE. The other polyolefin is a low-flow polypropylene (PP) grade Moplen® HP555G from Lyondell Basell Industries with a MFI = 1.3 g per 10 min (230 °C, 2.16 kg) and $T_m = 170$ °C.

2.2. Melt blending

In order to prepare the PVA/PP and PVA/PE blends, the respective pellets were dried, weighed and mixed by hand in a bag. A 26 mm co-rotating twin-screw scientific extruder (LTE 26–40, Labtech Engineering Co, Ltd, Thailand) was used for the melt blending. The temperatures from barrel zone to die zone were kept between 180 and 190 °C. The motor loading were kept at approximately 50%, and the pressure on the die was about 10 bar. The melt was extruded through a 3 mm two-strand die and pelletized afterwards. Finally, the pelletized granules were dried for 12 h at 80 °C and then used to produce dry films of blends (PVA/PP and PVA/PE, respectively).

2.3. Film production

Films were made in a sheet-extrusion line equipped with a single screw extruder (Zhangjiagang Chuangjie Plastic Machinery Co, Ltd, China), a slit die (100 mm × 0.8 mm) and downstream calendering rolls (Wayne 12 inch sheet line, Wayne Machine and Die Co, USA). Figure 1 shows the setup. The calender stage was used to reduce the thickness of the films and also to produce drawn films. The screw speed was 50–70 rpm and the screw torque around 50%. The extruder has four heating zones plus two for the die. The extruder zones were set to 180 °C and the die zone to 190 °C. Predrawing was

Figure 1. Left: single screw extruder with calender unit. Right: close-up view of the rear rollers.

Table 1. Designation and parameters of predrawn blends from polyvinyl alcohol (PVA) and polyolefins (PE and PP, resp.). λ_p is the predraw ratio. t_f is the film thickness.

PVA/PE (70 : 30)			PVA/PP (70 : 30)		
	λ_p	t_f (mm)		λ_p	t_f (mm)
AE10	1.0	0.52	AP10	1.0	0.70
AE22	2.2	0.39	AP22	2.2	0.32
AE40	4.0	0.22	AP43	4.3	0.27
AE75	7.5	0.18	AP60	6.0	0.16
AE96	9.6	0.16			

performed by increasing the rotation speed of the calender stage. The predraw ratio λ_p is the ratio of the film speed in the calender stage with respect to the film speed at the exit of the slit die. Table 1 presents the studied films and their macroscopic parameters.

2.4. Tensile testing

Dumbbell specimens S3 according to DIN 53504 are punched from the films using a toggle-lever press manufactured by Zwick, Ulm, Germany. The width of the specimen bar is 2 mm. For each oriented material the fiber axis of the sample is parallel to the direction of the test bar.

Testing is done in a self-made [22] tensile rig. A grid of fiducial marks is printed on the test bars [23]. The clamping distance is 20 mm. A 100 N load cell is used. Signals from load cell and transducer are recorded during the experiment. The sample is monitored by a TV camera. Video frames are grabbed every 10 s and are stored together with the experimental data. The machine is operated at a cross-head speed of 1 mm min^{-1}. Using the fiducial marks, the local macroscopic strain $\varepsilon = (\ell - \ell_0)/\ell_0$ is computed automatically from the average initial distance, ℓ_0, of the fiducial marks close to the point of x-ray irradiation and the respective actual distance, ℓ. The method that has been described earlier [24] fails for $\varepsilon \approx 0.6$. So a new method has been developed. Now the user encircles two fiducial marks in the first video frame. Then the program inverts the gray scale, computes the maximum intensity M_m inside the circle and selects all pixels with $M(i, j) > 0.8\, M_m$. The selected pixels form a spot. Its center of gravity (i_g, j_g) is computed. The distance between the centers of gravity of the two user-selected spots is ℓ_0. For the video frames that have been grabbed later at time t, the program tracks the user-selected circles by relocating them to the (i_g, j_g) that has been determined in the previous step. After the described spot analysis $\ell(t)$ is computed and $\varepsilon(t)$ is established.

The true stress, $\sigma = F/A$, is computed from the force F measured by the load cell after subtracting the force exerted by the upper sample clamp, and $A = A_0/(1+\varepsilon)$, the estimated actual sample cross-section. A_0 is the initial cross-section of the central zone of the test bar. The equation assumes conservation of the sample volume. The local strain rate is $\dot{\varepsilon} \approx 1.3 \times 10^{-3}\,\mathrm{s}^{-1}$. The tests are stopped when the sample begins to neck.

2.5. SAXS setup

Small-angle x-ray scattering (SAXS) is carried out in the synchrotron beamline A2 at HASYLAB, Hamburg, Germany. The wavelength of radiation is $\lambda = 0.15$ nm, and the sample-detector distance is 2560 mm. Scattering patterns are collected by a 2D marccd 165 detector (mar research, Norderstedt, Germany) in binned 1024×1024 pixel mode (pixel size: $158.2\,\mu\mathrm{m} \times 158.2\,\mu\mathrm{m}$). Scattering patterns of the PVA/PE are recorded every 60 s with an exposure of 50 s. Because the scattering of the PVA/PP materials is very weak, the patterns are recorded every 120 s with an exposure of 110 s. The patterns $I(\mathbf{s}) = I(s_{12}, s_3)$ cover the region $-0.24\,\mathrm{nm}^{-1} \leqslant s_{12}, s_3 \leqslant 0.24\,\mathrm{nm}^{-1}$. $\mathbf{s} = (s_{12}, s_3)$ is the scattering vector with its modulus defined by $|\mathbf{s}| = s = (2/\lambda)\sin\theta$. 2θ is the scattering angle. The patterns are normalized and background corrected [25]. This means intensity normalization for constant primary beam flux, zero absorption, and constant irradiated volume V_0. Because the flat samples are wider than the primary beam, the correction has been carried out assuming $V(t)/V_0 = (1/(1+\varepsilon(t)))^{0.5}$. The equation assumes constant sample volume. No radiation damage is observed.

2.6. SAXS data evaluation

The scattering patterns $I(\mathbf{s}) = I(s_{12}, s_3)$ are transformed into a representation of the nanostructure in real space. The only assumption is presence of a multiphase topology. The result is a multidimensional chord distribution function (CDF), $z(\mathbf{r})$ [26]. The method is exemplified in a textbook [27] and in the original paper [26] where figures show the change of the pattern from step to step. Here, we only summarize the steps and introduce the important quantities. The CDF with fiber symmetry in real space, $z(r_{12}, r_3)$, is computed from the fiber-symmetrical SAXS pattern, $I(s_{12}, s_3)$, of a multi-phase material. In order to compute $z(r_{12}, r_3)$, $I(s_{12}, s_3)$ is projected on the representative fiber plane. Multiplication by s^2 applies the real-space Laplacian. The density fluctuation background is determined by low-pass filtering. It is eliminated by subtraction. The resulting interference function, $G(s_{12}, s_3)$, describes the ideal multiphase system. Its 2D Fourier transform is the sought CDF. In the historical context the CDF is an extension of Ruland's interface distribution function (IDF) [28] to the multidimensional case or, in a different view, the Laplacian of Vonk's multidimensional correlation function [29]. The CDF is an 'edge-enhanced autocorrelation function' [30–33]—the autocorrelation of the gradient field, $\nabla\rho(\mathbf{r})$. $\rho(\mathbf{r})$ is the electron density inside the sample that is constant within a domain (crystalline, amorphous). Thus as a function of ghost displacement $\mathbf{r}$, the multidimensional CDF $z(\mathbf{r})$ shows peaks wherever there are domain *surface contacts* between domains in $\rho(\mathbf{r}')$ and in its displaced ghost $\rho(\mathbf{r}' - \mathbf{r})$. Such peaks $h_i(r_{12}, r_3)$ are called distance distributions [28]. Distance $\mathbf{r} = (r_{12}, r_3)$ is the ghost displacement. In this paper we track the few distance distributions that are present. We compute their position and their widths both in straining direction (meridional) and in transverse direction (equatorial) by fitting a bivariate polynomial to the cap of the peak. The method has been described in an earlier paper [24]. The studied peaks are the distance distributions of the domains (crystalline and amorphous superimposed), the long period distributions, and for the materials with microfibrillar structure a depletion peak that defines the shell zone of the microfibrils. From the fit of the cap we discuss the evolution of the center, i.e. the most-probable distance which can be a domain thickness d_m or a long period L_m and the lateral width of the peak (e_d or e_L) that describes the lateral extension of the considered entities. Unfortunately, the kind of corresponding average over the ensemble is unknown. Moreover, some distance distributions are extracted from the CDFs as curves from which the number-average dimensions of the corresponding entities ($\bar{d}(\varepsilon)$ or $\bar{L}(\varepsilon)$) are determined by integration and studied as a function of the macroscopic strain ε that is measured at the point where the x-ray beam irradiates the sample.

3. Results and discussion

3.1. Tensile data

Figures 2 and 3 present the stress–strain curves recorded during the straining experiments. All samples are strained in the orientation direction of the film. The experiments are stopped when the samples begin to develop a neck because from this time the SAXS pattern does not change any more. The homogeneous extensibility is longer in the predrawn materials than in the undrawn samples. The area under the stress–strain curve is a measure of toughness. For the PVA/PE blends, moderate predrawing ($\lambda_\mathrm{p} = 2.2$) increases the toughness. Further increase of λ_p leads to progressive decrease of the toughness, but only the material with the highest predraw ratio is somewhat softer than the original material.

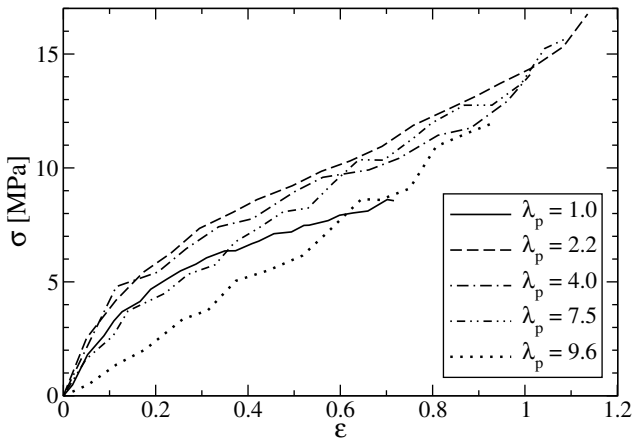

Figure 2. PVA/PE (70 : 30) blends, differently predrawn (predraw ratio λ_p). Stress–strain curves $\sigma(\varepsilon)$. Curves end where the material begins to develop a neck.

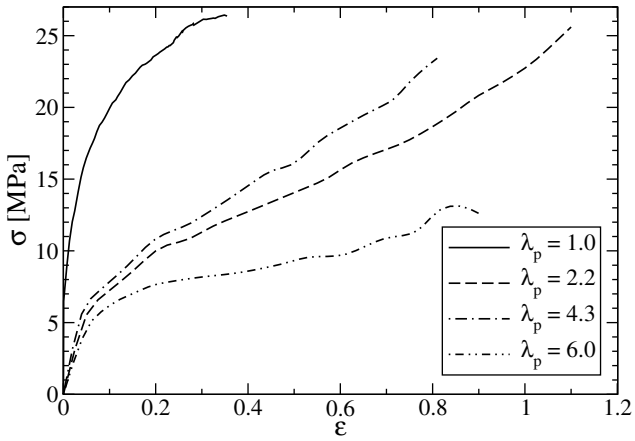

Figure 3. PVA/PP (70 : 30) blends, differently predrawn (predraw ratio λ_p). Stress–strain curves $\sigma(\varepsilon)$. Curves end where the material begins to develop a neck.

In contrast, all the predrawn PVA/PP materials are considerably softer than the undrawn material. This is a characteristic behavior [34] observed when highly oriented precursors of hard-elastic thermoplasts are drawn [15, 35]. This predrawing is known to cause a transformation of the amorphous layers that goes along with the formation of voids [18, 35, 36] and turns the plastic material into a (hard-)elastic material.

The end points of the curves from both kinds of blends demonstrate that necking starts at much higher strain than with

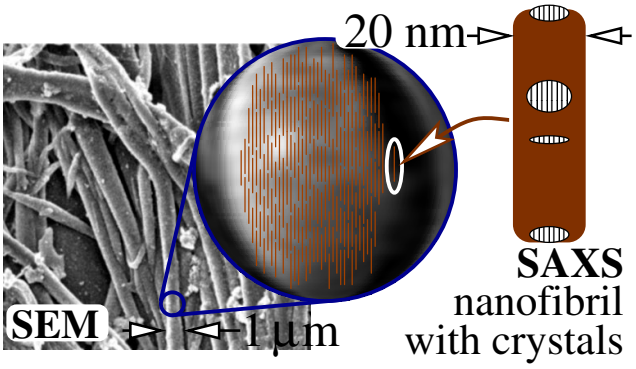

Figure 4. PVA/PP $\lambda_p = 6.0$. Left: washed-out PP microfibrils (diameters: 1–2 μm) in a SEM picture (size: 20 μm × 20 μm). Middle: the magnified part shows the swarm of nanofibrils embedded in the microfibril. The nanofibrils are probed by SAXS. Right: a nanofibril characterized by crystalline domains arranged in a row and surrounded by a depletion shell.

homopolymers of PE or PP. Moreover, predrawing further retards the formation of a neck.

3.2. Microfibrils and nanofibrils

Figure 4 presents an SEM picture showing the polypropylene microfibrils that are left over after partially washing out the PVA from drawn PVA/PP. The diameters of the microfibrils vary between 1 and 2 μm. As indicated in the magnifier image, these microfibrils are filled by a swarm of nanofibrils, and the SAXS is probing those nanofibrils. One of the nanofibrils is indicated on the right. Anticipating the results of the SAXS analysis, the diameter of the nanofibrils is in the order of magnitude of 20 nm. Each nanofibril is defined by a row of crystalline PP domains embedded in amorphous PP. This means that around each row of crystalline grains there is an amorphous depletion zone in which no crystalline grains are found. SEM pictures of the drawn PVA/PE blends look very similar. Anticipating the results from the mechanical tests in the synchrotron beam, only the PVA/PP blend reveals hard-elastic behavior. This is no contradiction to the similar microfibrillar structure seen in the SEM, because hard-elasticity is the consequence of a peculiar oriented structure on the nanometer scale, not on the scale of micrometers.

3.3. Measured SAXS patterns

The patterns change slowly, so it is sufficient to select a few patterns for demonstration. Figures 5 and 6 display the central part of selected SAXS patterns that have been recorded during the straining experiments. In figure 5 the evolution of the SAXS is unspectacular. With increasing strain ε, the envelope is deformed from circular to elliptic, and with increasing predraw ratio λ_p an equatorial streak and an equatorial lobe develop. Neither the PVA nor the PE cause the typical discrete SAXS of a semicrystalline polymer. A long period cannot be determined directly from the SAXS pattern. This is different with the PVA/PP blends. Figure 6 presents the corresponding patterns. The scattering of the undrawn material is presented

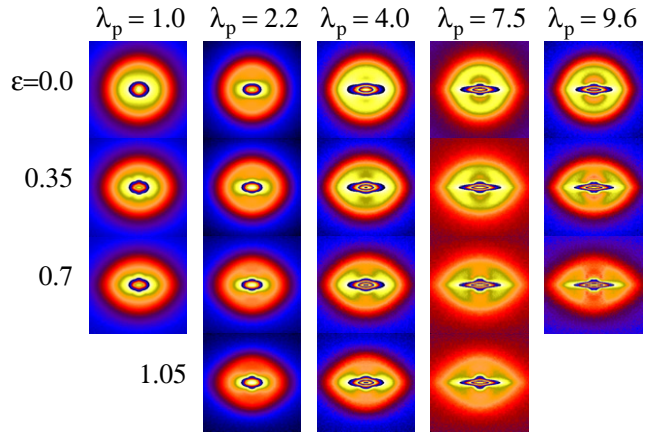

Figure 5. PVA/PE (70 : 30) blends with different predraw ratio λ_p. Observed SAXS patterns $I(s_{12}, s_3)$ as a function of the predraw ratio (horizontal) and the local macroscopic strain ε at the point of irradiation (vertical). All patterns are on the same logarithmic pseudo-color scale. The graphs show the region $-0.15\,\mathrm{nm}^{-1} \leqslant s_{12}, s_3 \leqslant 0.15\,\mathrm{nm}^{-1}$. The straining direction s_3 is vertical.

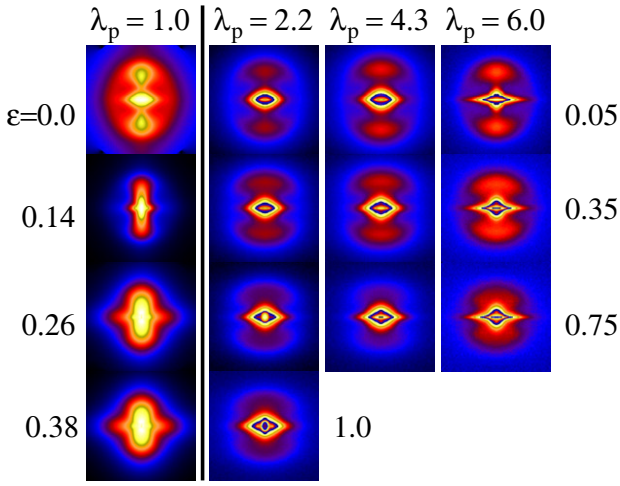

Figure 6. PVA/PP (70 : 30) blends with different predraw ratio λ_p. Observed SAXS patterns $I(s_{12}, s_3)$ as a function of the predraw ratio (horizontal) and the local macroscopic strain ε at the point of irradiation (vertical). The vertical black line discriminates between the two different scales of ε. All patterns are on the same logarithmic pseudo-color scale. The graphs show the region $-0.15\,\mathrm{nm}^{-1} \leqslant s_{12}, s_3 \leqslant 0.15\,\mathrm{nm}^{-1}$. The straining direction s_3 is vertical.

in the upper left corner. It shows the typical scattering of semicrystalline polypropylene with uniaxial orientation [22, 37, 38]. When unblended thermoplasts are sheet-extruded but not drawn, such a morphology is well known and called a precursor of a hard-elastic material [35]. It is the result of matching the molecular mass, the pressure gradient in the die, and the temperature gradient [15, 39]. Moderate cold drawing is known to turn the precursor hard-elastic.

In figure 6, the left row shows nanostructure evolution during the straining of sample AP10. Up to $\varepsilon = 0.14$ the SAXS intensity increases and the peak becomes narrower in the transverse direction. This indicates widening of the PP lamellae. Such widening can be explained by

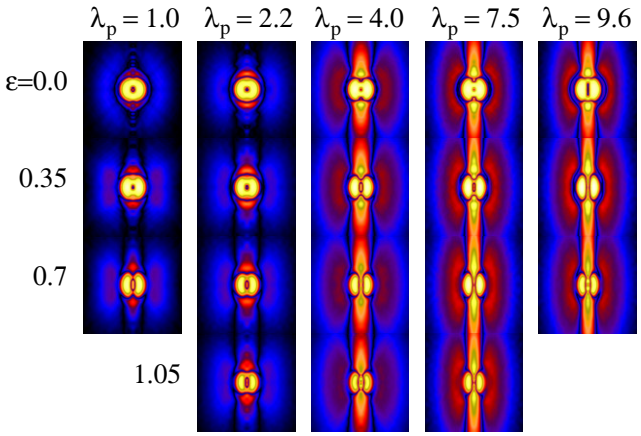

Figure 7. PVA/PE (70 : 30) blends with different predraw ratio λ_p. CDF patterns $|z(r_{12}, r_3)|$ computed from $I(s_{12}, s_3)$ as a function of the local macroscopic strain ε. All patterns are on the same logarithmic pseudo-color scale. The graphs show the region $-50\,\text{nm} \leqslant r_{12}, r_3 \leqslant 50\,\text{nm}$. The straining direction r_3 is vertical.

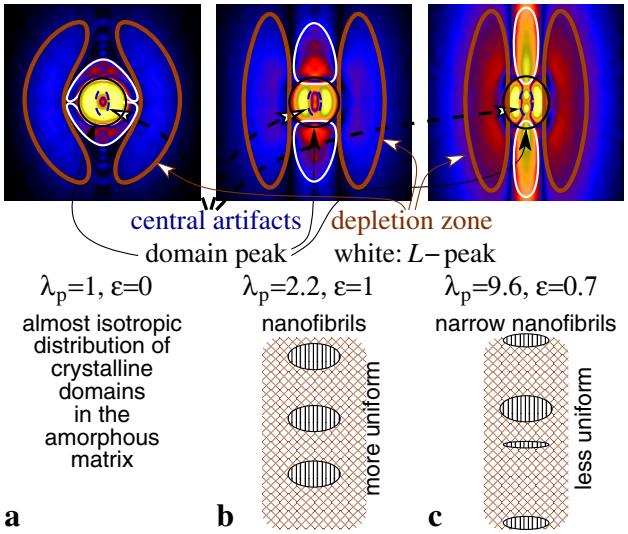

Figure 8. PVA/PE blends. Similar CDF features and the corresponding nanostructure. Central artifacts (small dashed ellipses) are found in every CDF. The central yellow region is the domain peak (encircled by a black ring). White borders mark the long-period peak, and brown borders mark the second domain peak (depletion zone). Below the CDFs, the corresponding nanostructure is described or sketched.

epitaxial strain-induced crystallization or by the detachment of cross-hatched lamellae. Vice versa, for higher strain the peaks grow wide, indicating a narrowing of the crystalline domains, possibly caused by fracture of the main lamellae. A more detailed description of the fracture mechanism is presented in the CDF analysis below.

3.4. Structure evolution in PVA/PE blends

CDFs computed from the SAXS patterns of the PVA/PE blends are presented in figure 7. The exhibited nanostructure appears rather simple. It is explained in figure 8, where the dominant features in the CDFs are marked. Sketches of the related nanostructure are presented. Before straining, the undrawn sample AE10 (figure 8(a)) it is almost isotropic. Nevertheless, its CDF already reveals all the features of the drawn samples. We assign the observed discrete scattering to the semicrystalline PE from the blend. The reason is that in the other set of materials (PVA/PP) the weak discrete scattering found is the typical scattering of neat PP. If we do not find discrete scattering of PVA in PVA/PP, then it is most probably also negligible in the PVA/PE blends.

Let us discuss the features of the PE nanostructure. The innermost elliptical mark in the three CDFs from figure 8 encircles the central artifacts. They arise from the limited area of the detector. Further out, a black mark encircles the domain peak. The innermost domain peak is the representation of the domain form factor in the CDF [27]. Because it is not related to the correlation between different domains, it is always found at smaller distances than the long-period peak. In figures 8(a) and (b) the domain peak appears circular. Thus, no anisotropy of the domains can be detected. This is different in figure 8(c). The elongated shape shows that either the crystalline domains or the amorphous regions appear elongated.

Let us now consider the peaks further away from the center. In the observed simple CDFs these are only the main long period (bordered by white lines) and a lateral domain peak far out that has been bordered by brown lines. In the virgin material AE10 (figure 8(a)) the orientation of these peaks is only moderate. It is almost perfect in the predrawn, respectively, strained materials (cf figures 8(b) and (c)). The long-period peak on the meridian is the only peak in these materials that is related to the arrangement of domains. These domains (crystalline grains) are arranged in rows that extend in the meridional direction, but there is only correlation between next neighbors. Such rows of crystalline grains are commonly called microfibrils [40, 41]. Instead, let us call them nanofibrils to discriminate them from the fibrillar entities that show up in SEM images (cf figure 4) of the studied samples.

In an intermediate state (figure 8(b)) the main L-peak on the meridian is still rather compact showing that the distances between the crystalline grains inside the nanofibrils do not vary extremely. Nevertheless, the second domain peak (encircled by brown lines) is already forming two bars to the left and to the right of the meridian. It describes the size distribution of a zone around the center of the nanofibril in which only amorphous PE material is found. Thus we propose to call the peak a depletion-zone peak. Its shape in the equatorial direction is the diameter distribution of the nanofibrils including the depletion shell. It changes little during the straining experiments on most of the PVA/PE samples. Results of a quantitative evaluation will be presented in figure 11.

With increasing ε, the L-peak turns into a streak along the meridian. This shows that the distances between the crystalline domains become increasingly irregular. Such extremely broad long-period distributions produce no discernible long-period peak in the SAXS pattern, but the feature is revealed in a CDF. Moving outward along the meridian, we observe that the breadth of the L-streak stays constant. This demonstrates that there is no correlation

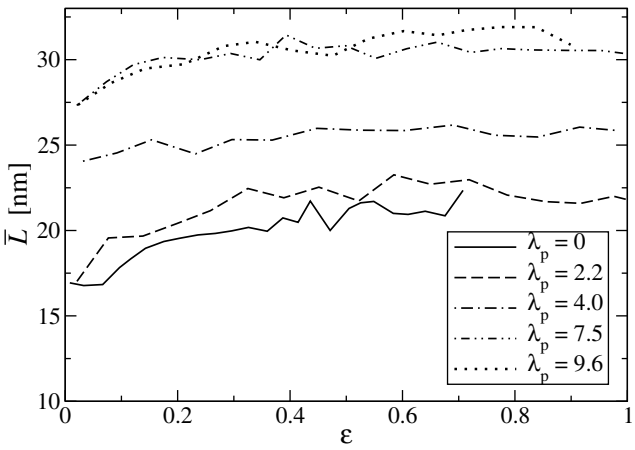

Figure 9. PVA/PE blends, differently predrawn (predraw ratio λ_p). The number-average long period $\bar{L}$ of the distribution of long periods as a function of both λ_p and the macroscopic strain ε in the test.

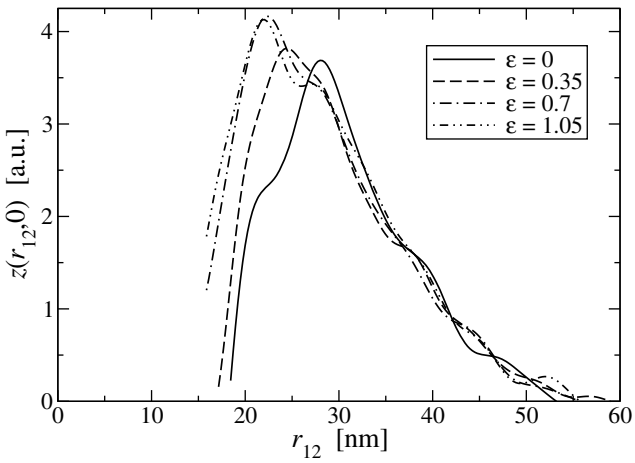

Figure 10. PVA/PE blend AE22 ($\lambda_p = 2.2$). Change of the profile of the depletion streak in the CDF as a function of strain ε for the only sample that shows a strong effect.

between the crystallite breadth and the distance between two of them.

For an approximative characterization of the response of the PE nanostructure on the mechanical load we have determined the most probable long period, L_m, from the position of the maximum of the long-period peak in the CDF. This is the value from the CDF that usually coincides with the long period determined from a long-period peak in the SAXS pattern, but here the measured SAXS stays diffuse. As a result, λ_p has no significant influence on L_m. The variation of L_m with ε is small also. Inspection of the long-period distribution in the meridional section of the CDF shows that increasing strain ε broadens the long-period distribution. The center of gravity of the long-period distributions is the number-average long period $\bar{L}$. Figure 9 presents the results. As a function of the predraw ratio λ_p, an increase of $\bar{L}$ is observed, but the curves from the two highest predraw ratios are almost identical. This finding indicates saturation. As a function of ε we observe a moderate increase of $\bar{L}$ up to $\varepsilon \approx 0.7$. Thus the data show that the swarm of nanofibrils resist straining, and possibly even the complete PE microfibrils act as semi-rigid fillers in the PVA matrix. From the curves the average longitudinal deformation

$$\varepsilon_l = \frac{\bar{L}(\varepsilon)}{\bar{L}(0)} - 1$$

of the nanofibrils is established. This parameter may be used to quantify the amount of rigidity in the straining direction.

In general, the diameter distribution of the nanofibrils inside the PE microfibrils does not change much as a function of applied strain. The exception is sample AE22. Figure 10 shows the evolution of the equatorial profile of the depletion streak in the CDF as a function of ε. The curves characterize the number distribution of the PE nanofibril diameters including the depletion shell in the surrounding blend. Remember that the SAXS is normalized to the irradiated volume. The right shoulder of all peaks is identical. With increasing strain the left shoulder increases

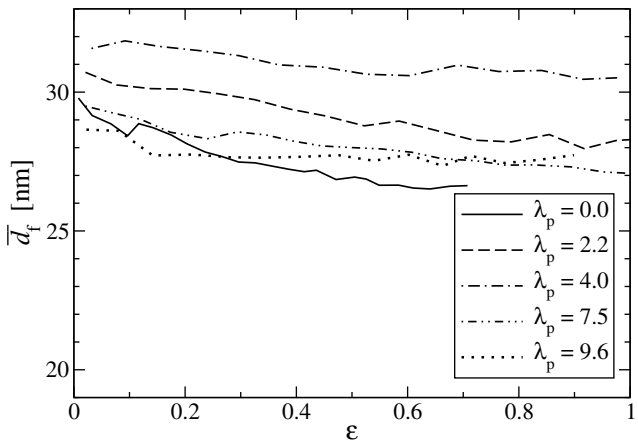

Figure 11. PVA/PE (70/30) blends, differently predrawn (predraw ratio λ_p). Variation of the diameter $\bar{d}_f$ of the PE nanofibrils as a function of strain ε and λ_p.

and grows inward. We do not observe a simple peak shift that would indicate lateral compression of a set of nanofibrils that is permanently visible in the discrete SAXS during the test. The one-sided broadening may be explained by a combination of peak shift and contrast increase. The contrast is the density difference between the density in the depletion zone and the averaged density in the nanofibril core. A different explanation would assume that the straining induces correlation between initially uncorrelated crystalline grains. In this manner, such new nanofibrils would start to contribute to the discrete SAXS with increasing ε. Thus with AE22 the response of the nanofibril diameters on strain is complex.

The centers of gravity

$$\bar{d}_f = \frac{\int r_{12}\, z(r_{12}, 0)\, \mathrm{d}r_{12}}{\int z(r_{12}, 0)\, \mathrm{d}r_{12}}$$

of the curves are approximate number averages $\bar{d}_f$ of the diameters of the visible PE nanofibrils. Figure 11 presents $\bar{d}_f$ for all PVA/PE materials as a function of strain. If, as a function of ε, the transverse profile of the depletion peak

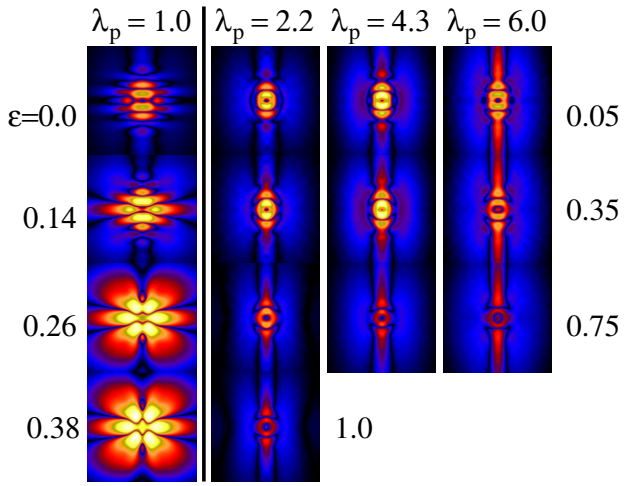

Figure 12. PVA/PP (70/30) blends, differently predrawn (predraw ratio λ_p). CDF patterns $|z(r_{12}, r_3)|$ computed from $I(s_{12}, s_3)$ as a function of the local macroscopic strain ε at the point of irradiation. The vertical line discriminates between the two different scales of ε. All patterns are on the same logarithmic pseudo-color scale. The graphs show the region $-50\,\text{nm} \leqslant r_{12}, r_3 \leqslant 50\,\text{nm}$. The straining direction r_3 is vertical.

(cf figure 10) shows a shift or at least a broadening, we could relate with sufficient significance the decrease of $\bar{d}_f(\varepsilon)$ to a transversal compression

$$\varepsilon_t(\varepsilon) = \frac{\bar{d}_f(\varepsilon)}{\bar{d}_f t(0)} - 1$$

of the PE nanofibrils. From this parameter we could discuss their lateral deformability. Finally, a suitable combination

$$V_f(\varepsilon)/V_f(0) = (\varepsilon_l(\varepsilon) + 1)(\varepsilon_t(\varepsilon) + 1)^2$$

of longitudinal and lateral deformability would result in a description of the volume change of the nanofibril during the straining process. This parameter can only be discussed if we assume that the observed ensemble of nanofibrils is permanent (i.e., no destruction or creation of SAXS-visible nanofibrils). The analysis shows that for the PVA/PE materials, $V_f(\varepsilon)/V_f(0) = 1$ is valid within the accuracy of the measurements. This result supports the suggestive statement that the nanofibrillar probes inside the PE microfibrils may somewhat deform under the load, but should keep their volume. A slight but significant variation is indicated only for the sample AE22 ($\lambda_p = 2.2$) that shows a distinct change of depletion streak profile (figure 10).

3.5. Structure evolution in PVA/PP blends

Figure 12 presents the CDFs computed from the SAXS patterns of the PVA/PP blends.

3.5.1. PVA/PP not predrawn. The left column presents the data from AP10, the material that has not been predrawn. Up to $\varepsilon \approx 0.2$, the CDFs predominantly exhibit the nanostructure of lamellar stacks with their principal axes oriented in straining direction. The streak on the equator carries a negative sign. It is thus related to long periods of domains arranged in the transverse direction. This feature is indicative for stacks of cross-hatched lamellae [22, 37, 42–46] in polypropylene. The corresponding domains are known to bridge the main lamellae. The first layer lines above and below the center of the CDFs describe the crystalline and amorphous domains (positive sign in the CDF). The second layer lines are the long periods (negative sign in the CDF). The (positive) domain peaks are much stronger and wider than the long period peaks.

The most probable long periods $L_m(\varepsilon)$ and domain positions $d_m(\varepsilon)$ have been determined from the positions of the peak maxima of the respective peaks in the CDF. In this way the macroscopic strain ε can be related to an approximation of the nanoscopic deformation. For the nanoscopic strain computed from the long period,

$$\varepsilon_{nL} = \frac{L_m(\varepsilon)}{L_m(0)} - 1,$$

the identity $\varepsilon_{nL} = \varepsilon$ holds. $L_m(0) = 13.8\,\text{nm}$. Thus the PP nanofibrils from inside the PP microfibrils do not behave as rigid fillers. They experience the macroscopic strain of the blend material. For the nanoscopic strain determined from the domain peak,

$$\varepsilon_{nd} = \frac{d_m(\varepsilon)}{d_m(0)} - 1,$$

the linear relation $\varepsilon_{nd} = 1.82\varepsilon$ holds ($d_m(0) = 6.2\,\text{nm}$). This indicates that the position of the maximum of the domain peak is governed by the expansion of the amorphous layers between the crystallites. Now let us estimate the quality of this approximation. We compute $d_c(0) = L_m(0) - d_m(0) = 7.8\,\text{nm}$. Assuming constant crystallite thickness we have

$$L_{me}(\varepsilon) = d_c(0) + (1.82\,\varepsilon + 1)\,d_m(0) \qquad (1)$$

for the expected long period. $\varepsilon = 0.38$ is the strain at the onset of necking. Then from equation (1) we obtain $L_{me}(0.38) = 18.3\,\text{nm}$, which is close to the measured value $L_m = 19.1\,\text{nm}$. This shows that the linear relations for $\varepsilon_{nL}(\varepsilon)$ and $\varepsilon_{nd}(\varepsilon)$ are compatible with the assumption that only the amorphous layers in the PP are subjected to strain. Nevertheless, varying the crystallinity in equation (1) shows that the significance of the two thicknesses d_c and d_a remains so low that we can only state that the crystallinity of the PP nanofibrils is between 40 and 60 vol.%.

The evolution of the lateral extensions of the domains and of the long periods are derived from the breadths of the meridional CDF peaks in the equatorial direction ($e_d(\varepsilon)$, $e_L(\varepsilon)$), and from the position $L_{cm}(\varepsilon)$ of the maximum of the equatorial peak that is related to the most probable distance between the bridging domains. The results are presented in figure 13. From $L_{cm}(\varepsilon)$ we can compute a nanoscopic cross-compression

$$\varepsilon_{nc}(\varepsilon) = \frac{L_{cm}(\varepsilon)}{L_{cm}(0)} - 1$$

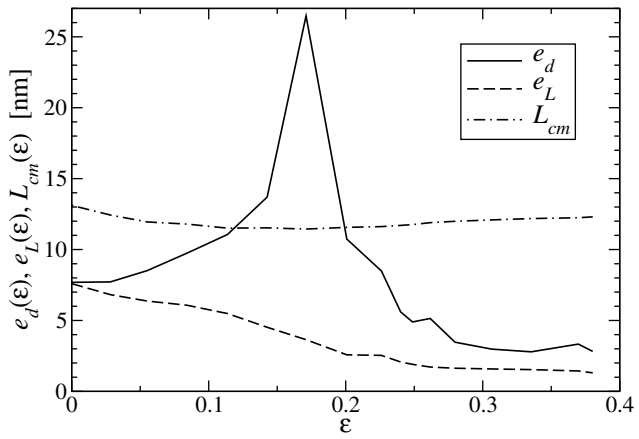

Figure 13. PVA/PP blend AP10 (not predrawn). Lateral extensions of the domains, $e_d(\varepsilon)$, of the stacks from two domains, $e_L(\varepsilon)$, and the distances between cross-hatched domains, L_{cm}.

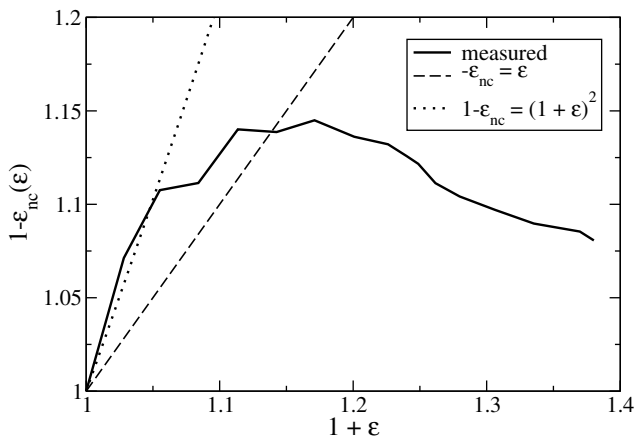

Figure 14. PVA/PP blend AP10 (not predrawn). Measured nanoscopic compression in cross-direction and theoretical curves for the shape of the crystallites that bridge the main lamellae. Dashed: bridging lamellae. Dotted: bridging struts.

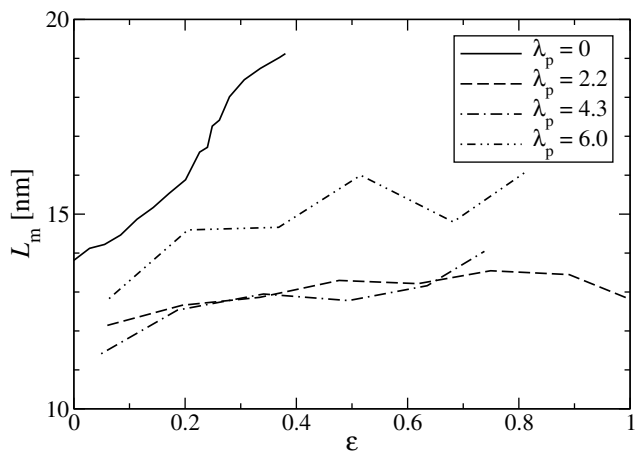

Figure 15. PVA/PP (70/30) blends differently predrawn (predraw ratio λ_p). The most-probable long period L_m as a function of both λ_p and the macroscopic strain ε.

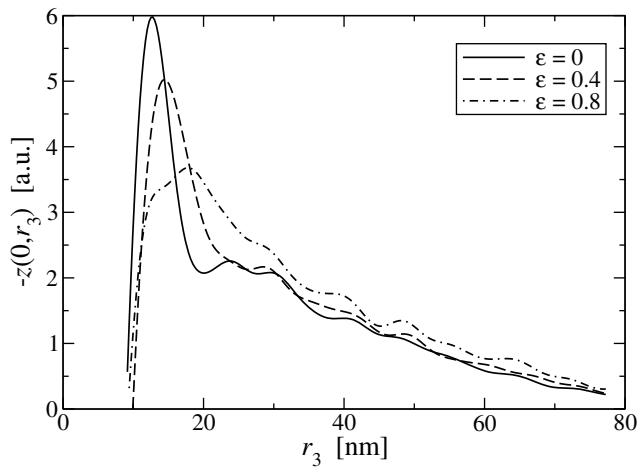

Figure 16. PVA/PP blend AP60 ($\lambda_p = 6.0$). Change of nanofibril long period distribution as a function of strain ε.

and compare it to ε. The shape of $\varepsilon_{nc}(\varepsilon)$ should be a function of the shape of the bridging crystallites. If the crystallites are flat (lamellae), one would expect $-\varepsilon_{nc}(\varepsilon) = \varepsilon$. If the crystallites are struts, one would expect $1 - \varepsilon_{nc}(\varepsilon) = (\varepsilon + 1)^2$ to a first approximation, if conservation of volume is assumed. Figure 14 presents the result. It shows that for very small ε the compression among the bridging domains is two dimensional, indicating that struts are detached from the main lamellae and compressed. For $\varepsilon > 0.04$ the curve drifts from struts to lamellae. At $\varepsilon = 0.14$ the global compression fits the notion of detaching lamellae from the main lamellae. From this point the CDFs begin to exhibit destruction of the original scaffold of interconnected PP lamellae. The curve cannot be discussed in a simple way anymore, because now the equatorial streak also begins to collect lateral correlations among fragments.

3.5.2. The predrawn PVA/PP blends. The CDFs of the predrawn PVA/PP materials (figure 12, row 2–4) look similar to the CDFs of the PVA/PE materials from figure 7. As with the PVA/PE materials, the predrawn PVA/PP samples exhibit a nanofibrillar structure. Figure 15 presents the most probable long periods $L_m(\varepsilon)$ as determined from the maxima of the long-period distributions. We present it because it is the value that is commonly determined from the maximum of a long-period peak in the SAXS. Figure 16 shows the complete long-period distribution for the sample with the highest predraw ratio. Respective graphs for the other PVA/PP materials look similar. We observe that the distribution is considerably skewed. The major effect of increasing strain appears to be a shift of the distribution to higher long periods. This is consistent with the notion of a uniform extensibility of nanofibrils with different long periods. The center of gravity of these distributions is the number-average long period $\bar{L}$. Figure 17 presents the curves $\bar{L}(\varepsilon)$ for the PVA/PP materials. At $\varepsilon \approx 0.2$ an increased rise of $\bar{L}$ is observed for all materials. From AP10 we know that this is the strain at which crystalline domains start to fail in great quantities. The samples with $\lambda_p = 0$ (AP10) and $\lambda_p = 2.2$ (AP22) exhibit a saturation long period $\bar{L} = 19$ nm before they start to neck visibly. AP22 shows a very long saturation plateau for $0.5 < \varepsilon < 1$. Thus in this interval the PP nanofibrils of AP22 can be considered rigid

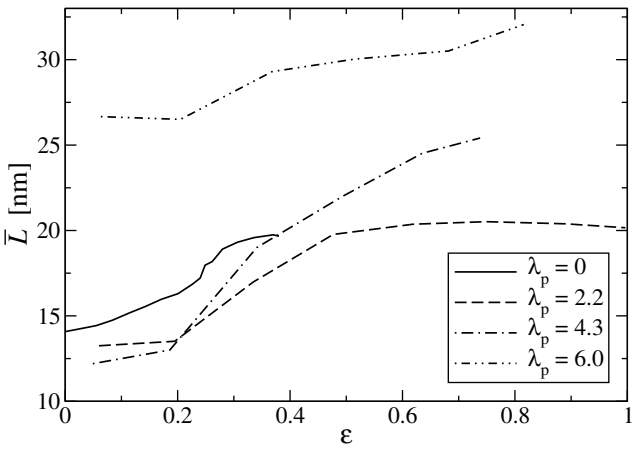

Figure 17. PVA/PP (70/30) blends, differently predrawn (predraw ratio λ_p). The number-average long period $\bar{L}$ of the distribution of long periods as a function of both λ_p and the macroscopic strain ε in the test.

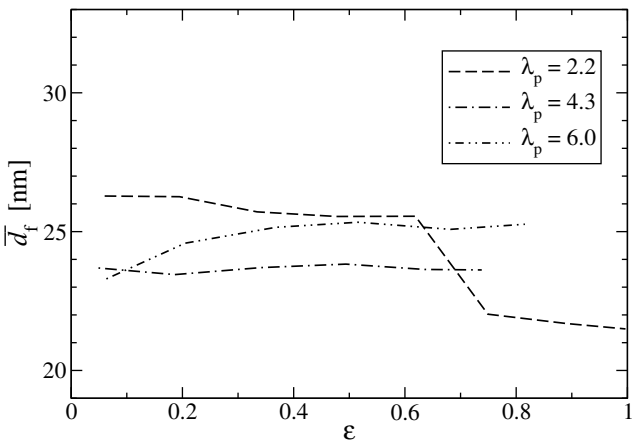

Figure 18. PVA/PP (70/30) blends, differently predrawn (predraw ratio λ_p). Variation of the average diameter $\bar{d}_f$ of the PP nanofibrils as a function of strain ε and λ_p.

after having been predrawn. In contrast, the PP nanofibrils from the materials with higher λ_p cannot be regarded as rigid. They appear more extensible than the PE nanofibrils from the corresponding PVA/PE blends. $\bar{L}(\varepsilon_{max})$ increases with increasing λ_p, similar to the behavior of the PVA/PE blends.

In the transverse direction the PP nanofibrils also respond to the applied strain. The peak shape remains constant, but with increasing ε a shift to the right is noticed for most of the PVA/PP materials. This is different to the PVA/PE materials where lateral compression but not lateral expansion of the nanofibrils has been the major response. Such diameter expansion upon strain can be explained by epitaxial strain-induced crystallization. Material at the edge of the crystallites that turns from amorphous to crystalline increases the lateral extension of each crystallite in the nanofibril. The diameter of the nanofibril grows. With PP, this phenomenon has been observed in previous work [47].

In order to quantify the effect, we compute the center of gravity of the nanofibril diameter distributions and obtain the number-average nanofibril diameter $\bar{d}_f(\lambda_p, \varepsilon)$. Figure 18

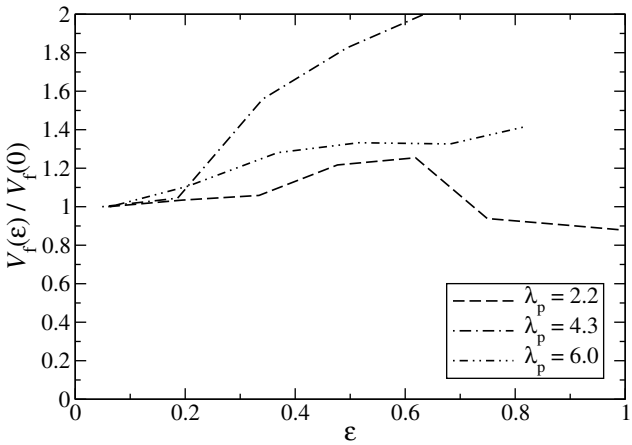

Figure 19. PVA/PP (70/30) blends, differently predrawn (predraw ratio λ_p). Volume change of the PP nanofibrils in the blend as a function of strain ε.

shows the result. A sudden decrease of $\bar{d}_f$ is observed for $\varepsilon > 0.6$ in the material with the lowest predraw ratio. This decrease can be explained by the fracture of crystalline domains. Related to the macroscopic data this failure happens at $\sigma \approx 15$ MPa, and this stress is 25% lower than the breaking stress for PP crystallites that has been found in previous work [38, 47]. Unfortunately we cannot determine the microscopic stress on the PP microfibrils which may differ from the macroscopic stress.

Finally, let us assess the volume change of the representative PP nanofibril in the straining test. As demonstrated in figure 17, the peak areas do not change considerably. This shows that with the PP scattering we most probably view the same ensemble of probes throughout the straining process and the straightforward interpretation of the volume variation parameter appears justified. Figure 19 presents the result. Obviously the volume of the semicrystalline PP nanofibrils in the blends increases considerably with increasing ε for the highly predrawn materials. As already pointed out, the reason is probably strain-induced crystallization. This means that amorphous PP in the depletion zone around the nanofibril turns crystalline. In this way volume increases, filled with arranged domains of crystalline and amorphous material.

This re-arrangement requires little change of the total crystallinity, because the amorphous zones between the crystallites also contribute to the volume of the nanofibrils. It is even possible that the overall crystallinity does not change at all, if simultaneously isolated small crystallites are destroyed, because they can neither be detected by WAXS or SAXS. Tracking of crystallinity changes by differential scanning calorimetry (DSC) would require application of deformation calorimetry [48], a delicate method that is rarely applied these days. In particular if only the smaller fraction in a blend is elastic, the detection of the faint signal would be a challenge. For pure hard-elastic polypropylene, Gritz and Mller [48] carried out deformation calorimetry and reported a net increase of crystallinity.

A diameter increase is not found with the PE nanofibrils. One might argue that a conversion that may go along with a

change of average density of the PP may put some extra stress on the bonding zone between the two polymers in the blend.

4. Conclusions

We have characterized extruded blends from PVA and polyolefins in mechanical tests. Simultaneously, the evolution of the nanostructure has been monitored. The two different kinds of blends exhibit different evolution of structure and different mechanical properties, even though all materials contain 70% PVA. Thus for the mechanical properties, the properties of this matrix polymer are of less importance than those of the embedded polyolefin. In predrawn films both the embedded polyolefins form microfibrils. However, they respond differently to mechanical load. While PVA/PE shows the expected stiffening compared to unstrained films, PVA/PP unexpectedly appears softer. The reason is a fundamental structural difference in the extruded films. Before straining the PE microfibrils exhibit an isotropic semicrystalline nanostructure, whereas the PP microfibrils show the highly oriented semicrystalline structure typical for a precursor of a hard-elastic thermoplast (PHET). The production of a PHET from a neat polymer requires the proper choice of molecular mass of the polymer and skillful choice of processing parameters (pressure and temperature gradient in the die). We imagine that in blend processing another parameter may be important: the ratio of the volume expansion coefficients of the matrix polymer (PVA) and the polyolefin (PP or PE) may modify the effective pressure in the polyolefin droplet.

In our experience, an important factor that makes the material turn microfibrillar is the relatively cold drawing of the film after the extrusion stage [49–51]. Important roles may also be played by the difference in the solubility parameters of the components, the saponification degree of the PVA, and the degree of branching of the polyolefins.

Our results show, obviously, that polyolefins can be transferred into a PHET, even if they only represent the minority fraction in a blend. It is well known that the hard-elastic properties of the material emerge after predrawing the PHET. This conversion is observed in the PVA/PP blend, in which the PP exhibits the structure of a 'precursor of hard-elastic polypropylene' (PHEPP). Notably, the conversion into hard-elastic polypropylene (HEPP) is observed when the blend is predrawn. An extraction of the PP microfibrils is not necessary. Thus the mechanical coupling between the PVA matrix and the PP microfibrils appears to be sufficient.

The HEPP microfibrils can be easily washed out by water. In this shape, hard-elastic material might be interesting for special applications. We assume that even other thermoplastic materials may be converted into hard-elastic microfibrillar material by tuning the chemistry, the physical parameters, and the processing parameters.

Processing a neat polymer, the transformation from the precursor to the hard-elastic material causes void formation and whitening of the material. This is not the case in the predrawn blend. Neither the material becomes turbid, nor the SAXS develops the strong void scattering that is typically observed during the conversion. We suppose that the reason is the low diameter of the embedded microfibrils. The proximity of the interface may attenuate void formation, and void propagation is stopped after a short distance. Here we probably observe one of the scaling effects that indicate the transition from a classical material to a nanomaterial.

Acknowledgments

The authors thank the Hamburg Synchrotron Radiation Laboratory (HASYLAB) for beam time granted in the frame of project I-2011-0087. Xuke Li is acknowledged for his assistance during the beam time.

References

[1] Fakirov S, Evstatiev M and Friedrich K 2000 From polymer blends to microfibrillar reinforced composites *Polymer Blends* vol 2, ed D R Paul and C B Bucknall (New York: Wiley-Interscience), chapter 33, p 455
[2] Ku T H and Lin C A 2005 *J. Polym. Res.* **12** 23
[3] Ku T H and Lin C A 2005 *Textile Res. J.* **75** 681
[4] McGarel O J 2005 Smokable polymeric casing *Patent Application* US 2005/0163948 A1
[5] Jang J and Lee D K 2003 *Polymer* **44** 8139
[6] Bunn C W 1948 *Nature* **161** 929
[7] Assender H E and Windle A H 1998 *Polymer* **39** 4295
[8] Cho J D, Lyoo W S, Chvalun S N and Blackwell J 1999 *Macromolecules* **32** 6236
[9] Miyazaki T, Hoshiko A, Akasaka M, Shintani T and Sakurai S 2006 *Macromolecules* **39** 2921
[10] Sugiyama M and Maeda Y 1995 *J. Phys. Soc., Japan* **64** 1002
[11] Kanaya T, Ohkura M, Kaji K, Furusaka M and Misawa M 1994 *Macromolecules* **27** 5609
[12] Lyoo W S, Chvalun S, Ghim H D, Kim Pil J and Blackwell J 2001 *Macromolecules* **34** 2615
[13] Zeinolebadi A, Stribeck N, Ganjaee Sari M, Dencheva N, Denchev Z and Botta S 2012 *Macromol. Mater. Eng.* **297** 1102
[14] Johnson M B and Wilkes G L 2001 *J. Appl. Polym. Sci.* **81** 2944
[15] Noether H D 1979 *Intern. J. Polym. Mater.* **7** 57
[16] Johnson M B and Wilkes G L 2002 *J. Appl. Polym. Sci.* **83** 2095
[17] Xu J, Johnson M and Wilkes G L 2004 *Polymer* **45** 5327–40
[18] Lee S Y, Park S Y and Song H S 2006 *Polymer* **47** 3540
[19] Kuraray 2012 Thermoplastic processing of Mowiol/PVOH (www.kuraray-am.com/pvoh-pvb/downloads/Mowiflex_TC_232_Introduction.pdf)
[20] Kuraray 2012 Mowiflex TC—thermoplastic processing (www.kuraray-am.com/pvoh-pvb/downloads/Mowiflex_TC_232_Processing.pdf)
[21] Dorigato A and Pegoretti A 2012 *Colloid Polym. Sci.* **290** 359–370
[22] Stribeck N, Nöchel U, Funari S S and Schubert T 2008 *J. Polym. Sci. Polym. Phys.* **46** 721
[23] Stribeck N 2009 Deformation behavior of nanocomposites studied by x-ray scattering: instrumentation and methodology *Nano- and Micromechanics of Polymer Blends and Composites* vol 1, ed J Karger-Kocsis and S Fakirov (Munich: Hanser) chapter 8, p 269
[24] Denchev Z, Dencheva N, Funari S S, Motovilin M, Schubert T and Stribeck N 2010 *J. Polym. Sci. B: Polym. Phys.* **48** 237
[25] Stribeck N 2007 *X-ray Scattering of Soft Matter* (Heidelberg: Springer)
[26] Stribeck N 2001 *J. Appl. Cryst.* **34** 496

[27] Stribeck N 2007 *X-ray Scattering of Soft Matter* (Heidelberg: Springer) section 8.5.5
[28] Ruland W 1977 *Colloid Polym. Sci.* **255** 417
[29] Vonk C G 1979 *Colloid Polym. Sci.* **257** 1021
[30] Debye P and Bueche A M 1949 *J. Appl. Phys.* **20** 518
[31] Porod G 1951 *Colloid Polym. Sci.* **124** 83
[32] Vonk C G 1973 *J. Appl. Cryst.* **6** 81
[33] Baltá Calleja F J and Vonk C G 1989 *X-ray Scattering of Synthetic Polymers* (Amsterdam: Elsevier)
[34] Park I K and Noether H D 1975 *Colloid Polym. Sci.* **253** 824
[35] Sprague B S 1973 *J. Macromol. Sci. Phys.* **B8** 157
[36] Noether H D and Whitney W 1973 *Colloid Polym. Sci.* **251** 991
[37] Stribeck N, Nöchel U, Almendárez Camarillo A, Roth S V, Dommach M and Bösecke P 2007 *Macromolecules* **40** 4535
[38] Stribeck N, Zeinolebadi A, Ganjaee Sari M, Botta S, Jankova K, Hvilsted S, Drozdov A, Klitkou R, Potarniche C G, Christiansen J D and Ermini V 2012 *Macromolecules* **45** 962
[39] Jordens K, Wilkes G L, Janzen J, Rohlfing D C and Welch M B 2000 *Polymer* **41** 7175
[40] Porod G 1961 *Fortschr. Hochpolym.-Forsch.* **2** 363
[41] Peterlin A 1971 *J. Mater. Sci.* **6** 490
[42] Compostella M, Coen A and Bertinotti F 1962 *Angew. Chem.* **74** 618
[43] Sakthivel A and Abhiraman S 1984 *J. Appl. Polym. Sci.* **29** 4257
[44] Norton D R and Keller A 1985 *Polymer* **26** 704
[45] Olley R H and Bassett D C 1989 *Polymer* **30** 399
[46] Ganjaee Sari M, Stribeck N, Moradian S, Zeinolebadi A, Bastani S and Botta S 2012 *Polym. Int.,* at press DOI:10.1002/pi.4399
[47] Stribeck N, Nöchel U, Funari S S, Schubert T and Timmann A 2008 *Macromol. Chem. Phys.* **209** 1992
[48] Göritz D and Müller F H 1974 *Colloid Polym. Sci.* **252** 862
[49] Evstatiev M and Fakirov S 1992 *Polymer* **33** 877
[50] Dencheva N, Oliveira M J, Carneiro O S, Pouzada A S and Denchev Z 2010 *J. Appl. Polym. Sci.* **115** 2918
[51] Stribeck N, Bhattacharyya D and Fakirov S 2012 Structural and mechanical characterization of the micro- and nanofibrillar reinforcement of precursors of polymer-polymer composites *Synthetic Polymer–Polymer Composites* vol 1, ed D Bhattacharrya and S Fakirov (Munich: Hanser) chapter 16, p 563